Urban Climate 49 (2023) 101500

Contents lists available at ScienceDirect

Urban Climate

journal homepage: www.elsevier.com/locate/uclim

Downscaling mapping method for local climate zones from the perspective of deep learning

Wenbo Yu[a], Jun Yang[a,b,c,*], Feng Wu[d,**], Baojie He[e], Huisheng Yu[a], Jiayi Ren[a], Xiangming Xiao[f], Jianhong(Cecilia) Xia[g]

[a] School of Humanities and Law, Northeastern University, Shenyang 110169, China
[b] Jangho Architecture College, Northeastern University, Shenyang 110169, China
[c] Human Settlements Research Center, Liaoning Normal University, Dalian 116029, China
[d] Key Laboratory of Regional Sustainable Development Modeling, Institute of Geographic Sciences and Natural Resources Research, CAS, Beijing 100101, China
[e] Centre for Climate-Resilient and Low-Carbon Cities, School of Architecture and Urban Planning, Chongqing University, Chongqing 400045, China
[f] Department of Microbiology and Plant Biology, Center for Earth Observation and Modeling, University of Oklahoma, Norman, OK 73019, USA
[g] School of Earth and Planetary Sciences (EPS), Curtin University, Perth 65630, Australia

A R T I C L E I N F O

Keywords:
Local climate zone
Refinement mapping
Optimal mapping scale analysis
Deep learning model optimization
Geographic information system

A B S T R A C T

Increased attention has been paid to refining Local Climate Zone (LCZ) maps. However, the mapping process is difficult because of image resolution limitations and the lack of detailed planning data. To our knowledge for the first time, to promote the application of refined LCZ maps in urban climate research, we have proposed the downscaling mapping process by by integrating GIS workflow and remote sensing workflow. The results have shown that: (1) By adjusting the scale and input of the deep learning model, the LCZ basemap achieved the highest overall accuracy of 83.64% and the highest data matching degree of 0.71. (2) Visual interpretation showed that the overall accuracy of LCZ map at all scales is >70%, and the highest overall accuracy of 84.44% is achieved at 20 m scale. (3) Usefulness assessment showed that the LST levels of LCZs significantly differ at all scales ($p < 0.01$). The 160 m scale was the most suitable for analysis of the thermal characteristics of urban landscapes. This downscaling mapping method will help urban planners in developing urban climate models to determine the impact mechanisms of urban development and support progress in sustainable urban development efforts.

1. Introduction

Rapid urbanization and climate change are important global trends (Zhang, 2020). The population in global cities have increased weekly by ~1 million people and urban areas have expanded by ~20,000 American football fields per day (Zhu et al., 2019a). Pursuit of a better life is at the heart of urbanization (Stokes and Seto, 2019). However, as the most pronounced local climate phenomenon in urbanization, the urban heat island effect is often accompanied by adverse effects such as increased urban air pollution (Liang et al., 2021), a surge in the energy demand (Li et al., 2019; Yang et al., 2020a), and increased risk of residents' heat stress (Li et al., 2018;

* Corresponding author at: Jangho Architecture College, Northeastern University, Shenyang 110169, China.
** Corresponding author.
E-mail addresses: 2110013@stu.neu.edu.cn (W. Yu), yangjun8@mail.neu.edu.cn (J. Yang), wufeng@igsnrr.ac.cn (F. Wu), 1810019@stu.neu.edu.cn (H. Yu), 2210011@stu.neu.edu.cn (J. Ren), xiangming.xiao@ou.edu (X. Xiao), c.xia@curtin.edu.au (J. Xia).

https://doi.org/10.1016/j.uclim.2023.101500
Received 10 December 2022; Received in revised form 22 February 2023; Accepted 12 March 2023

Vanos et al., 2015). This poses considerable challenges in the sustainable development of cities. Based on the Sustainable Development Goals (United Nations, 2015), building sustainable cities and communities and taking climate action are important for achieving peace and prosperity for people and our planet. To promote achieving the Sustainable Development Goals, urban climatologists are committed to establishing local climate responses to urbanization and planning a more climate-resilient urban sustainable development blueprint (Chen et al., 2023; He et al., 2019; Masó et al., 2019; Woodruff et al., 2022).

The Local Climate Zone (LCZ) (Stewart and Oke, 2012; Stewart et al., 2014) is a useful concept for determining the influence of urban landscape changes on local heat island effects (illustrations and real scenes are shown in Table S1 in Support material). Urban landscapes have been divided into ten built types and seven natural types according to the material, surface coverage, structure, and energy metabolism. This highlights the difference in the thermal environment between different landscape types. The LCZ concept focuses on distinguishing urban climate patterns without considering specific regional and cultural characteristics. Therefore, it is more easily transferable than landscape classification methods such as urban topographic zones (Ellefsen, 1991), urban land units (Stokes and Seto, 2019), and global urban footprints (Esch et al., 2013). The LCZ concept has been widely used in thermal environment analysis (Ren et al., 2022; Yu et al., 2023), outdoor thermal comfort improvement (Stepani and Emmanuel, 2022), and urban heat island effect mitigation (Li et al., 2021; Yang et al., 2020b). Its effectiveness in addressing the impact of urban climate hotspots, such as urban ventilation (Yang et al., 2021a), energy consumption and water balance (Brousse et al., 2016), and carbon emissions has been demonstrated (Jarvi et al., 2019).

GIS workflow is a common means of LCZ mapping using computer technology. Lelovics et al. (2014) and Unger et al. (2014) were the first to use GIS workflow for LCZ mapping. Since then, studies applying GIS workflows for mapping have been conducted in >20 cities worldwide (Quan and Bansal, 2021). LCZ mapping of GIS workflows generally relies on detailed planning data such as building vector and land cover data. Increasing the data density is an effective way of improving the mapping accuracy (Ren et al., 2023; Xin et al., 2023). Therefore, many studies have incorporated additional parameters into LCZ mapping. This has included the application of digital elevation and remote sensing image data to supplement the description of urban surface properties (Estacio et al., 2019). Vegetation description information has also been added to improve the classification accuracy of vegetation-type LCZs (Geletič and Lehnert, 2016; Oliveira et al., 2020). However, there is a lack of coherent global urban databases suitable for urban climate research (Chen et al., 2021), especially in certain developing countries and regions. These areas are expected to experience substantial population migration from rural to urban areas in the next few years (Zhou et al., 2018). Their rapid urbanization process needs to rely on LCZs and the promotion of urban climate monitoring and improvement. However, urban data resources and especially building height information often have low spatial and temporal resolutions or are imperfect or missing.

Remote sensing (RS) workflow is another commonly used method for LCZ mapping which is used to directly extract LCZ classification information from Earth observations (Ma et al., 2021). Compared with GIS workflows, the transferability of RS workflows is considerably enhanced. However, this method requires a high-confidence LCZ label dataset as training data (Qiu et al., 2022). World Urban Database and Access Portal Tools (WUDAPT) currently represents the primary platform for global LCZ classification. WUDAPT officially released global LCZ L0-level maps generated on the LCZ online generation platform based on the random forest algorithm (Demuzere et al., 2019, 2020). Deep learning methods are also gaining attention for LCZ classification. Convolutional neural networks can effectively employ the receptive field to capture and learn necessary contextual information (Rosentreter et al., 2020). Compared with the method provided by WUDAPT, it pays more attention to understanding the target scene, which can improve the overall accuracy by 6–8% and the built type accuracy by 10–13% (Yoo et al., 2019). Researchers have committed to promoting convolutional neural networks to play more important roles in global LCZ mapping. Based on convolutional neural networks, researchers have established many LCZ-specific classification networks including Sen2LCZ (Qiu et al., 2020), LCZNet (Liu and Shi, 2020), and MSMLA (Kim et al., 2021). Based on the Sentinel-2 satellite images with 10 m spatial resolution, a LCZ label dataset named So2Sat LCZ42 (Zhu et al., 2019b) comprising 42 metropolitan areas with different cultures and development levels worldwide was also established for global LCZ mapping. However, the LCZ map generated by the RS workflow needs to have the same grid size as the training data. This means that adjustment of the grid scale of the LCZ map under the CNN method needs to be based on the reevaluation of the LCZ label dataset at the same scale, which relies heavily on unified urban knowledge.

The fusion of GIS and RS workflows promotes more refined and accurate development of LCZ mapping. At this stage, LCZ mapping studies that integrate both workflows have predominantly focused on using GIS data as an optional input for RS workflows to improve the classification accuracy (Kim et al., 2021; Yoo et al., 2020). However, the flexibility of GIS workflows in handling the LCZ grid scale has often been overlooked. Therefore, as an alternative, we have proposed a downscaling process for the LCZ base map, which was generated by deep learning based on the GIS method. This process uses RS workflow to make up for the obstacles caused by urban data with low spatial and temporal resolutions and provides more complete urban architectural landscape information. However, the process uses GIS workflow to obtain more flexible and refined mapping results and is no longer limited by the grid scale of the fixed label dataset. This means that it can be adapted to urban climate research under different grid scale requirements. We believe that the downscaling process facilitates the application of more refined LCZ maps in urban climate studies and will help urban planners in determining the mechanisms based on which urban development affects local climate and how this can contribute towards sustainable urban development.

2. Data and methods

2.1. Data

2.1.1. Study area

The capital of Liaoning Province, Shenyang is in Northeast China. Shenyang has a temperate continental monsoon climate with four distinct seasons. The study area comprised the central area of Shenyang, which lies between 123.02°E–123.81°E and 41.46°N–42.19°N and included five subdivisions (Dadong, Huanggu, Shenhe, Tiexi, and Heping), Yuhong District, Shenbei New District, Hunnan District, and Sujiatun District (Fig. 1). As the capital of Liaoning Province, Shenyang has a well-developed society and economy. In 2020, the resident population of the study area was 7,885,100, the study area was 3495 km^2, and the population density was 2256.11 people/km^2. In the urban area of the study area, more intensive land use is achieved by building medium- and high-rise buildings (LCZ 1–2, 4–5) and large low-rise buildings (LCZ 8). In contrast, the suburbs are characterized by rural areas dominated by construction land for low-rise buildings. Shenyang is also an important heavy industry base in China, with equipment manufacturing as its pillar industry and numerous industrial parks (LCZ 10). Shenyang municipal district is located on the Songnen Plain. The landscape is predominantly characterized by agricultural land (LCZ D), with low forest cover and a concentration in the east of the municipal district (LCZ A-C). The Hun River (LCZ G) passes through the center of the municipal district and plays an important role in cooling the city.

2.1.2. Data source

The public LCZ label dataset So2Sat LCZ42 was used in this study for deep learning model training. It contains 400,673 Sentinel-1,2 image patches with a scale of 320 m from 42 metropolitan areas worldwide. The dataset is based on a strict LCZ labeling process with an overall confidence level of 85%.

The input data of the deep learning model are the product of Sentinel 2 RS images from four seasons generated by the Google Earth Engine (GEE) platform. The 10 m resolution Environmental Systems Research Institute (ESRI) Land Cover data (Karra et al., 2021) downloaded from GEE provide a finer segmentation of the natural landscape. The building outline vector data from the study area in 2020 were obtained from the National Tibetan Plateau Data Center (Zhang et al., 2022). The specific data sources and descriptions have been provided in Table 1 (see Table S2 in the Support material for the unique identifiers of the remote sensing images).

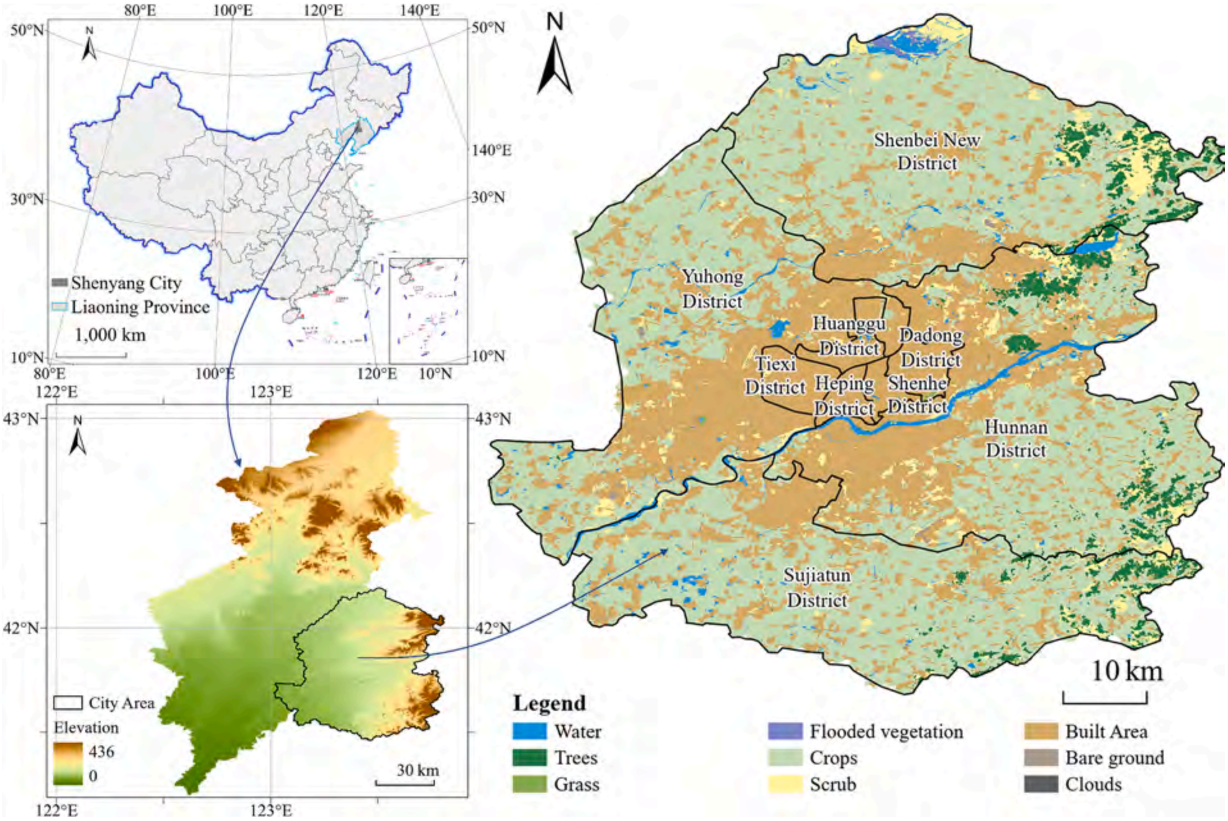

Fig. 1. Overview of the study area. (a) Location of Shenyang in China; (b) Topography and location of Shenyang municipal district; (c) Land cover of Shenyang.

Table 1
Data sources and descriptions.

Data type	Data source	Describe	Date
So2Sat LCZ42	http://doi.org/10.14459/2018mp1483140	LCZ label dataset	2018
Sentinel-2 RS images	https://earthengine.google.com/	Input for LCZ deep learning classification model	2020.01.14, 2020.05.13 2020.08.21, 2020.10.30
Landsat-8 RS images	https://earthengine.google.com/	LST retrieval	2020.07.22
Esri Land Cover	https://earthengine.google.com/	10 m resolution fine land cover products	2020
Building data	http://doi.org/10.11888/Geogra.tpdc.271702	Building outline vector	2020

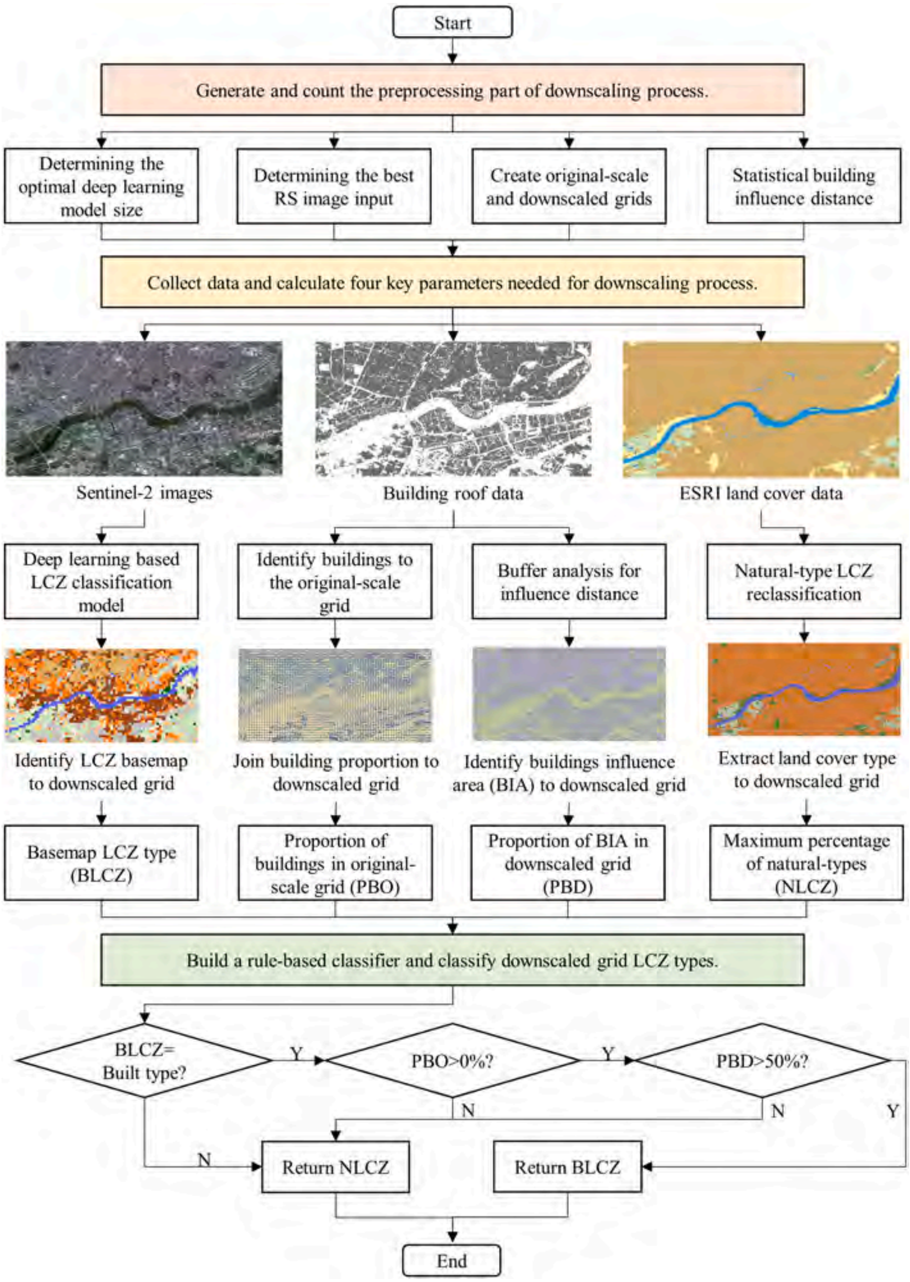

Fig. 2. Technical workflow chart of the downscaling process.

2.2. Methods

2.2.1. LCZ downscaling process

In this study, a LCZ downscaling mapping process was designed (Fig. 2). First, the downscaling process was preprocessed, which included the following steps: (1) Determine the optimal deep learning model scale suitable for the So2sat LCZ42 dataset according to the overall accuracy; (2) Compare the matching degree of the LCZ classification results generated by the RS images of the four seasons and determine the best input for the LCZ classification in the study area; (3) Use the fishing net tool in GIS to establish the original-scale grid of the same scale as the So2sat LCZ42 dataset; (4) Determine downscaling multiples and generate the downscaled grid; and (5) Calculate the median value of the influence distance of buildings according to the building outline data.

The four key parameters required for the downscaling process were calculated and connected to the downscaled grid, which included the following steps: (1) Select the deep learning model input with the highest matching degree to generate the LCZ basemap (BLCZ); (2) Identify the building outline of the original scale grid and calculate the building proportion (PBO) of the original scale grid

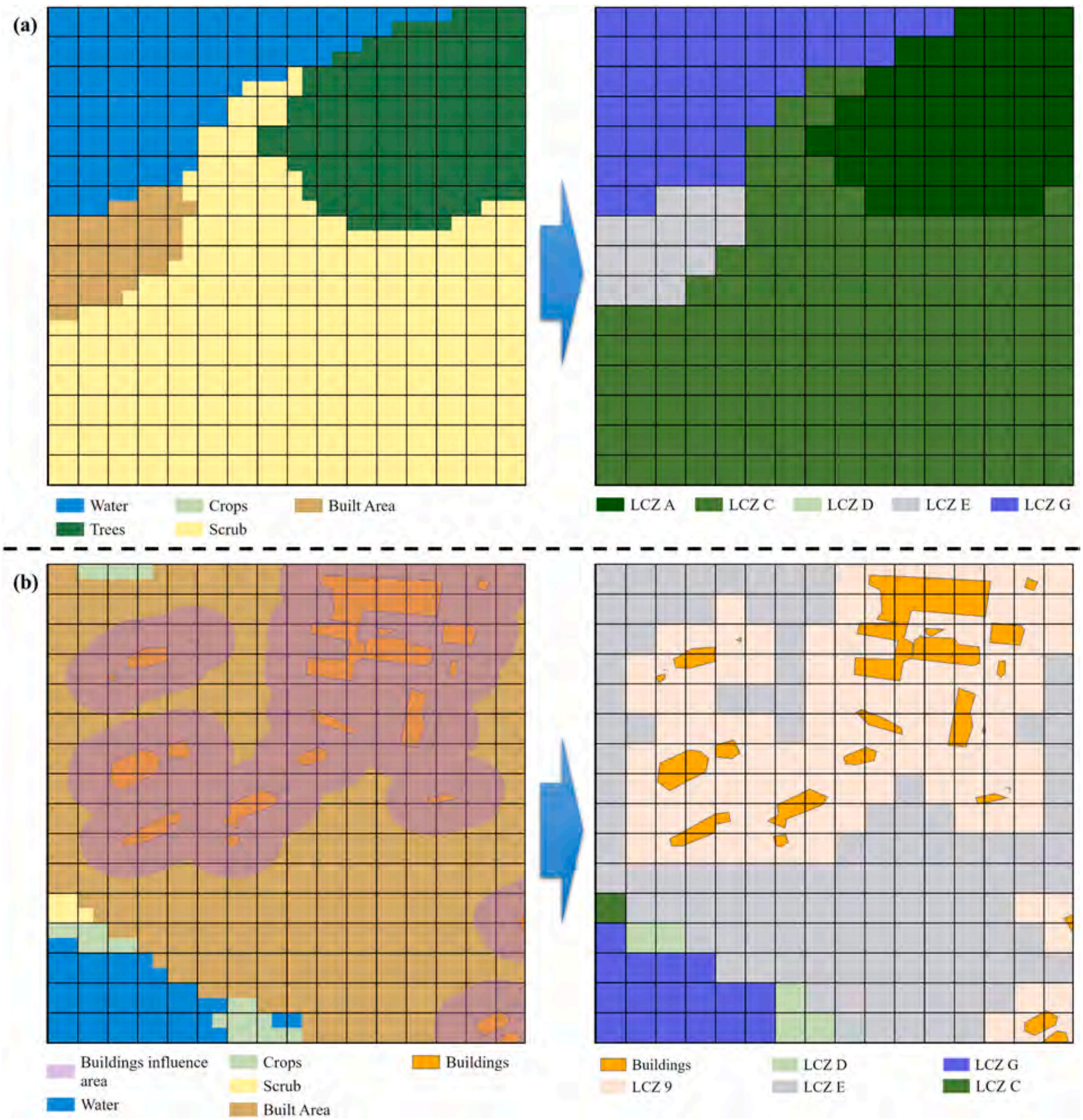

Fig. 3. Downscaling process of original scale grids with different LCZ types.

to determine if the built type LCZ grids were correctly classified; (3) Use the buffer analysis tool to generate the building influence area and calculate the proportion of the building influence area in the downscaled grid (PBD) to determine if the downscaled grid belongs to the built-type LCZ; (4) Reclassify ESRI Land Cover data into refined natural-type LCZs based on their characteristics and determine the natural LCZ type (NLCZ) with the largest proportion in the downscaled grid.

A rule-based classifier was constructed, and four key parameters were used to classify the downscaled grid LCZ type. Based on BLCZ, the original scale grid was divided into built type and natural type for downscaling. Fig. 3 shows the processing basis and downscaling results when the original scale grid has been scaled down by 16 times. If the original scale grid where the downscaled grid is located (BLCZ) belongs to the natural type, then the classifier determines the land cover type with the highest proportion (NLCZ) in each downscaled grid as the downscaled LCZ type. This is based on the 10 m resolution ESRI land cover data. As shown in Fig. 3(a), the original scale grid of BLCZ type LCZ A has been further divided into LCZ A, LCZC, LCZ D, LCZ E, and LCZ G according to the highest proportions of land cover types (NLCZ). If the original scale grid where the downscaled grid is located (BLCZ) belongs to the built type, we first determined whether the BLCZ of the grid had been incorrectly divided by determining whether the PBO is 0. If PBO was 0, we could not obtain the building information to determine the downscaled grid that belonged to the built type in the original scale grid. Therefore, the grid was then processed according to the downscaling process of the natural type original scale grid, that is, the reduced downscaled grid type is NLCZ. If the PBO is not 0%, the original scale grid can be further downscaled to built and natural types. The original grid scale (320 m) can guarantee the homogeneity of its internal built types (Lau et al., 2015; Zheng et al., 2018; Ching et al., 2019). Therefore, we believe that all the buildings in the original scale grid belong to the same built LCZ type. Buildings can have an impact on the local climate within a certain range. The buildings and their surrounding influencing area within a certain range jointly constitute the built LCZ type (Gal and Unger, 2009; Skarbit et al., 2017; Unger et al., 2014). The classifier will make the following judgment accordingly. If the proportion of buildings and their influenced areas in the downscale grid (PBD) is higher than that of the natural cover, the downscale grid type can be considered as built type LCZ. To achieve this, an effective method is to determine whether the PBD is higher than 50%. Fig. 3(b) shows the downscaling process of a grid with an original scale grid type of LCZ 9. The classifier will determine whether the PBD in each downscale grid is higher than 50%. If the PBD is higher than 50%, the downscaled grid reflects the built LCZ type of the original scale grid, and the downscaling type is BLCZ, that is, LCZ9. If the PBD is lower than 50%, the downscale grid is dominated by natural cover. Therefore, the classifier will follow the downscale process of natural type LCZ to assign the downscaled grid to the NLCZ type. In Fig. 3 (b), these grids have been further classified from LCZ 9 into LCZ C, LCZ D, LCZ E and LCZ G.

2.2.2. *LCZ basemap generation method*

In the downscaling process, the LCZ basemap generated based on deep learning provided the basis for distinguishing the built/natural type LCZ and the type and height attributes of the underlying surface of the built landscape. This plays an important role in the entire process. Improving the accuracy of the LCZ basemap is important in enhancing the validity of the downscaled map. As mentioned in the Section 2.2.1, in this study, the accuracy of the LCZ basemap was improved by optimizing the model size and inputs. The specific process is as follows.

2.2.2.1. Model selection and training process. The Multi-Scale, Multi-Level Attention Network (MSMLA-NET) has outperformed other networks with respect to the LCZ classification task, and was used for deep learning training of the LCZ label dataset (Kim et al., 2021). Fig. 4 shows that the MSMLA model comprises the backbone network Se-ResNet, Multi-Scale module, and Multi-Level Attention module. The MS module is suitable for scene classification and uses local information by fusing multiple viewpoints of input images at different scales. A smaller receptive field can then be used to extract fine features from local information, whereas a larger receptive field can be used to delineate spatial context features from global information. The convolutional block attention module (CBAM) is

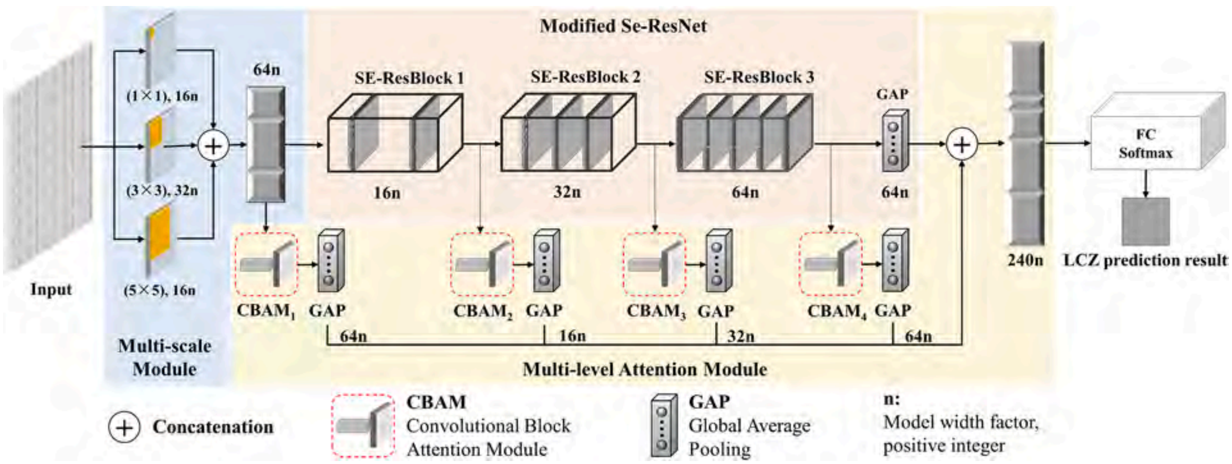

Fig. 4. MSMLA architecture (adapted from Kim et al., 2021).

integrated into the MLA module and the CBAM attention mechanism is divided into two parts, that is, spatial attention and channel attention. After CBAM, the new features will be assigned attention weights in the channel and spatial dimensions. This substantially improves the connection of each feature in the channel and spatial dimensions and is more conducive to extracting the effective features of the target. The model width factor *n* controls the overall parameter of the model and is used to optimize the size of the model.

The So2Sat LCZ42 dataset was used for deep learning training. The original training, validation, and test sets contain landscape information from different geographically separated cities. To learn more urban landscape information, the dataset was reorganized in this study. To form a new training dataset, 95% of the original training set and 80% of the validation set were randomly selected. The remaining parts of the training and validation sets were combined to form a new validation set, whereas the test set remained unchanged. During the training process in this study, the learning rate was dynamically adjusted and the training was stopped in advance. The initial learning rate was set to 0.01 and the verification accuracy of each iteration was checked. If the accuracy decreased, the learning rate was reduced ten times to continue training. If the validation accuracy dropped in both iterations, the training process was stopped.

2.2.2.2. Accuracy test. Given that the number of image patches and source complexity of the So2sat LCZ42 label dataset are higher than those of the original study (Kim et al., 2021), the MSMLA model size was adjusted by increasing the model width factor n to determine the optimal model width for this dataset. The overall accuracy (OA) measures the performance of the model with respect to the overall classification of LCZs and is the ratio between the number of LCZs that the model correctly predicted among all test sets to the overall number. It can be expressed as follows:

$$\mathrm{OA} = \sum_{i=1}^{M} \frac{LCZ_{ii}}{N}, \tag{1}$$

The overall accuracy of the built types, $\mathrm{OA_b}$, and the overall accuracy of natural types, $\mathrm{OA_n}$, measure the performance of the model with respect to the LCZ classification of built and natural types, respectively, and can be expressed as:

$$\mathrm{OA}_b = \sum_{i=1}^{M_b} bLCZ_{ii} \Big/ N_b \tag{2}$$

The overall class accuracy OA_{type} measures the ability of the model to effectively distinguish natural from built types and can be expressed as follows:

$$\mathrm{OA}_{type} = \frac{N - T}{N}, \tag{3}$$

The average accuracy (AA) measures the average value of user's accuracy. It can be expressed as follows:

$$\mathrm{AA} = \left(\sum_{i=1}^{\mathrm{M}} \frac{LCZ_{ii}}{LCZ_{i+}} \right) \Big/ M, \tag{4}$$

The average reliability (AR) measures the average value of user's accuracy. It can be expressed as follows:

$$\mathrm{AR} = \left(\sum_{i=1}^{\mathrm{M}} \frac{LCZ_{ii}}{LCZ_{+i}} \right) \Big/ M, \tag{5}$$

Kappa coefficient is a common indicator for consistency inspection, and its calculation method is as follows

$$\mathrm{Kappa} = \frac{N \sum_{i=1}^{\mathrm{M}} LCZ_{ii} - \sum_{i=1}^{M} (LCZ_{i+} \times LCZ_{+i})}{N^2 - \sum_{i=1}^{M} (LCZ_{i+} \times LCZ_{+i})}, \tag{6}$$

where, N is the total number of image blocks in the test set, and N_b and N_n represent the total number of image blocks of built and natural types in the test set, respectively. M is the number of LCZ types in the test set, and M_b and M_n are the number of categories of built and natural types, respectively. LCZ_{ii} refers to the diagonal elements of the confusion matrix, $bLCZ_{ii}$ and $nLCZ_{ii}$ represent the diagonal elements of built-type LCZs and natural-type LCZs in the confusion matrix, respectively. LCZ_{i+} is the total observation number of row I and LCZ_{+i} is the total observation quantity of the column. T is the sum of the number of image blocks whose natural type is classified as built type and the number of image blocks whose built type is classified as natural type in the confusion matrix.

2.2.2.3. Matching degree test. Urban land cover significantly changes depending on the season. To determine the effects of seasonal factors on the LCZ classification, ESRI Land Cover and building vector data were used to test the matching degree of the LCZ deep learning results in different seasons and select the best input. In the ESRI Land Cover category, the built area is LCZ 1–10 and LCZ E. Trees are considered LCZ A/B; shrubs are LCZ C. Grass, flooded vegetation, and crops are considered to be LCZ D, bare ground is considered to be LCZ F, and water is considered to be LCZ G. The land cover classification matching degree MD_{Lc} in the study area can then be expressed as follows:

$$MD_{Lc} = LC_{correct}/LC_{total}, \tag{7}$$

where $LC_{correct}$ indicates the number of grids with correct land cover classification and LC_{total} represents the number of all grids in the study area.

The urban built-up area is the main area for urban residents to carry out social and economic activities and the built form has a pronounced impact on the thermal environment (Yang et al., 2021b). Therefore, the building density in the grid was compared with that defined by the LCZ framework definition in this study to express the classification effect of the built-type LCZ. The matching degree of the building density MD_{BD} can be expressed as follows:

$$MD_{BD} = BD_{correct}/BD_{total}, \tag{8}$$

where $BD_{correct}$ represents the number of grids with correct building density classification and BD_{total} represents the number of grids containing building vector data in the study area.

The comprehensive matching degree MD of the LCZ map can be expressed as:

$$MD = k_1 MD_{LC} + k_2 MD_{BD} \tag{9}$$

where $k_1 = k_2 = 0.5$.

2.2.3. Building influence distance calculation

Gal and Unger (2009), Skarbit et al. (2017), and Unger et al. (2014) delineated the area of influence closest to the building by establishing a Thiessen polygon for the building and used this area as the influence range of the building. In this study, buildings and their impact areas were considered regular rectangles, and the median influence distance of the buildings was determined as follows:

$$d = \left(\sqrt{A/r} - \sqrt{a/r}\right)\Big/2, \tag{10}$$

where d is the median value of the building influence distance, A is the median value of the Thiessen polygon area, a is the median value of the building area, r is the median value of the building aspect ratio in the study area, and $\sqrt{A/r}$ and $\sqrt{a/r}$ represent the length of the short side of the Thiessen polygon and building rectangle, respectively. Based on modeling and calculations, the average impact distance of buildings in the study area was determined to be 28.3 m.

2.2.4. Usefulness assessment of the LCZ map

The usefulness of LCZ mapping remains a necessary and diverse research problem in this field. This study assessed the usefulness of the classification results through the ability of LCZ to distinguish urban landscape thermal characteristics (Zhao et al., 2017, 2021). In previous studies, the usefulness of LCZ maps was assessed using the station-observed air temperature (Kotharkar and Bagade, 2018a), mobile-measured air temperature (Leconte et al., 2015), or RS land surface temperature (LST; Quan, 2019). In these assessment methods, RS technology creates conditions for easy acquisition of the LST and urban surface heat island (Voogt, 2021). Therefore, in this study, RS data were used to analyze the significance of the LST differences between LCZ classes at different grid scales to assess the usefulness of the downscaling mapping results.

The atmospheric correction method was used for the land surface temperature retrieval of the Landsat-8 RS image. The thermal infrared radiance value L_λ consists of three parts, that is, the real radiated energy of the ground passing through the atmosphere, the upward radiated energy and the reflected energy of the downward radiated radiation reaching the ground. The formula is shown as follows

$$L_\lambda = [\varepsilon \cdot B(T_s) + (1-\varepsilon)L_\downarrow] \cdot \tau + L_\uparrow, \tag{11}$$

where τ is the atmospheric transmittance in the thermal infrared band, ε is the surface specific emissivity, T_s is the real temperature of the land surface, and $B(T_s)$ is the black body radiance.

The radiance $B(T_s)$ of a black body with temperature T can be calculated by the formula Eq. (12):

$$B(T_s) = [L_\lambda - L_\uparrow - \tau \cdot (1-\varepsilon)L_\downarrow]/\tau \cdot \varepsilon, \tag{12}$$

where, transmittance τ, atmospheric upward radiance $L_\uparrow$ and atmospheric downward radiance $L_\downarrow$ can be calculated by entering image information (center latitude and longitude, acquisition time) and the weather conditions (altitude, air temperature, atmospheric pressure, relative humidity) on the NASA official website. T_s is obtained with Planck's formula Eq. (11):

$$T_s = K_2/ln(K_1/B(T_s) + 1), \tag{13}$$

where, for Band 10 of Landsat 8 images, K_1=774.89 W/(m^2*μm*r) , K_2=1321.08 K.

Subsequently, 20% of the grids in LCZ maps were randomly selected as samples. The one-way analysis of variance (ANOVA) test and post-hoc pairwise comparison of Tamhaini T2 provided in SPSS 26 were used to determine = whether there was a significant difference in the LST among the LCZ types.

3. Results

3.1. Downscaling preprocessing results

3.1.1. Optimal model size

MSMLA models with different model width factors were used to learn the So2sat LCZ42 dataset. The test set evaluation results are presented in Table 2. MSMLA models can achieve an OA of >80%, >75% of AA and AR, and OA_{type} is higher than 98%. The classification ability for natural types is higher than that for built types. The OA_b is maintained above 75%, whereas OA_n is higher than 90%. With the increase in model width, OA, OA_b, and Kappa increase. When the model width factor was 4, the highest OA, OA_b, and Kappa of 83.64%, 78.68% and 82.09%, respectively, were achieved for the test set. When the model width factor was 5, the model was overfitting and OA, OA_b and Kappa all decreased. Therefore, MSMLA*4 was used as the optimal deep learning model in this study.

The confusion matrix of the test set generated by the MSMLA*4 model is shown in Fig. 5. Among the built types, LCZ 8 (large low-rise) has the highest accuracy rate, whereas LCZ 10 (heavy industry) has the lowest accuracy rate. Compact LCZ types (LCZ 1–3) can be easily confused with open LCZ types (LCZ 4–6) of the same height class. Open LCZ types (LCZ 4–5) can be easily confused when identifying building heights. Given that LCZ 8 and LCZ 10 exhibited a large low-rise morphology, confusion between the two was relatively easy.

3.1.2. Optimal model input

The input images and prediction results of the MSMLA*4 model for different seasons are presented in Fig. 6 and the matching degree of the prediction results is shown in Table 3. Seasonal factors influenced the LCZ prediction results. The winter LCZ map barely classifies the grids correctly, with an MD of 0.23. The natural and built types were largely misidentified as waterbodies and large low-rise buildings, respectively. This is predominantly because of the study area generally being covered with snow in winter, which disturbs the LCZ prediction. The spring LCZ map also has a low degree of land cover matching. This is mainly affected by rice planting in the study area. Several grids with notable farmland characteristics (LCZ D) were incorrectly identified as waterbodies, resulting in a MD_{LC} of 0.74. The results of the land cover identification based on the summer and autumn LCZ maps were relatively accurate, with a MD_{LC} value of 0.84 and 0.85, respectively. However, there was a considerable difference in determining the underlying surface attributes. Under the influence of vegetation phenology, more built grids in the autumn LCZ map were identified as compact type with more patches. Meanwhile, more built grids in the summer LCZ map were identified as open type with fewer patches. The results of the building density matching have shown that the summer LCZ map more accurately reflected the building characteristics. The highest MD_{BD} value was 0.57. Based on the results summary, natural land cover and building information was reflected well based on the application of the summer RS image for LCZ prediction, and the highest matching degree of 0.71 was obtained. Therefore, we chose the summer RS image as the deep learning input to generate the base map during downscaling.

3.2. LCZ downscaling mapping

The LCZ basemap obtained by deep learning was downscaled by integer multiples (1, 2, 4, 8, 16) using the downscaling process, and LCZ maps with grid scales of 320–20 m (Fig. 7b–f) were obtained. Comparison of the results of different downscaling LCZ maps has shown that the LCZ type of 70.66% of the grids is consistent across the maps at all scales, indicating that the downscaling process has a high level of stability. Grids in which the types have changed are predominantly distributed inside the built type LCZs or at the junctions of different types of LCZs. The downscaling method enables the extraction of hidden natural surface features within the built type grids. As the downscaling factor increases, the number of grids in which types change decreases. The boundaries between different LCZ types become smoother, and more refined changes in the underlying surface can be identified.

We created a total of 180 random points (20 for each district) to evaluate the accuracy of the LCZ maps at various scales, and the results are shown in Table 4. The 20-m scale LCZ map had the highest classification accuracy, while the 320-m scale LCZ map had the lowest classification accuracy. In previous studies, because RS workflow requires more image information to achieve high-precision classification, the optimal classification scale was substantially larger (150 m for Berlin, 170 m for Hamburg, 190 m for Cologne and Frankfurt, 480 m for Shanghai and Beijing) (Liu and Shi, 2020; Rosentreter et al., 2020). The downscale LCZ mapping method proposed in this study effectively improves the classification accuracy of the fine-scale LCZ map by introducing GIS workflow and more detailed building and land cover data.

Table 2
Overall accuracy of the MSMLA under different model width factors.

Model	n	Parameters	OA	OA_b	OA_n	OA_{type}	AA	AR	Kappa
MSMLA	1	808,913	81.37	74.99	90.87	98.22	76.04	76.14	79.61
MSMLA*2	2	3,148,809	82.07	76.31	90.64	98.23	76.74	77.02	80.37
MSMLA*3	3	7,020,097	82.04	76.43	90.41	98.25	76.64	76.61	80.35
MSMLA*4	4	12,422,777	83.64	78.68	91.04	98.11	77.81	78.13	82.09
MSMLA*5	5	19,356,849	82.92	77.23	91.39	98.12	78.02	77.71	81.30

Note: The unit of OA, OA_b, OA_n, OA_{type}, AA, AR, and Kappa is %.

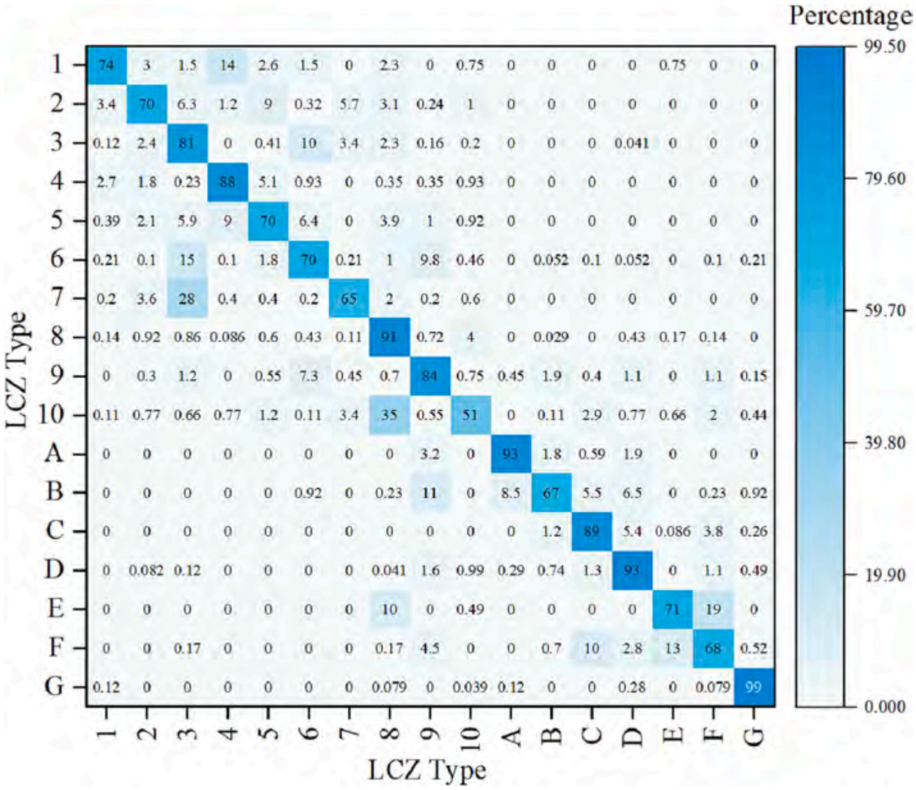

Fig. 5. MSMLA*4 confusion matrix.

3.3. Assessment of the usefulness of the LCZ downscaled map

The LCZ plays an important role because it can distinguish the LST between different landscapes. To assess the usefulness of the LCZ map, this paper first retrieved the LST of the study area through atmospheric correction method. The spatial LST distribution obtained from Shenyang is shown in Fig. 8. After that, the LST and its corresponding LCZ types at different scales are sampled at an interval of 20 m, and >11 million sampling points were obtained. The average value and standard deviation of LST of each LCZ type at different scales were statistically summarized, as shown in Table 5. Given that 70.66% of the grid LCZ types in all the scale maps are consistent, the average LST of the LCZs at different scales did not significantly differ. The highest and lowest LST values of the natural types were obtained for LCZ F and LCZ G, respectively. The highest and lowest LST values of the built types were observed for LCZ 2 and LCZ 9, respectively.

In this study, 20% of the grids were randomly selected as samples. The one-way ANOVA test provided in SPSS 26 and post-hoc pairwise comparison of Tamhaini T2 were used to determine whether there is a significant difference in the LST among the LCZ types. The one-way ANOVA test results have shown that the LST levels of LCZ at each scale significantly differed ($p < 0.01$), indicating that the LCZ downscaling process has a strong ability to express the thermal characteristics of urban landscapes. The post-hoc pairwise comparison results are shown in Fig. 9. In 136 pairs of paired comparisons, 5–6 pairs of LCZ have not significant LST differences at the 0.01 level. This also shows that the LST differences between different LCZ types can be effectively distinguished by the downscale maps. The proportions of LCZ 7 (lightweight low-rise) and LCZ F (bare soil or sand) are small in the study area, resulting in the least prominent landscape thermal characteristics among the study results. The LSTs of three LCZ combinations at the 160 m scale did not significantly differ at the 0.05 level, which is the most suitable scale for analyzing the urban thermal environment in the study area. The 200 m scale is the optimal scale to distinguish the characteristics of Hong Kong's thermal environment (Lau et al., 2015). This study has further demonstrated the applicability of the results in other cities with dense high-density buildings.

4. Discussion

4.1. Refined LCZ mapping and application

Stewart and Oke (2012), the creators of the LCZ concept, recommend 400–1000 m as the grid scale for LCZ maps. However, in practical applications, the grid scale of LCZ maps often varies from tens of meters to several kilometers based on the complexity of the urban surface and the study scale. Obtaining more refined edge recognition between LCZ classes is conducive to a more accurate

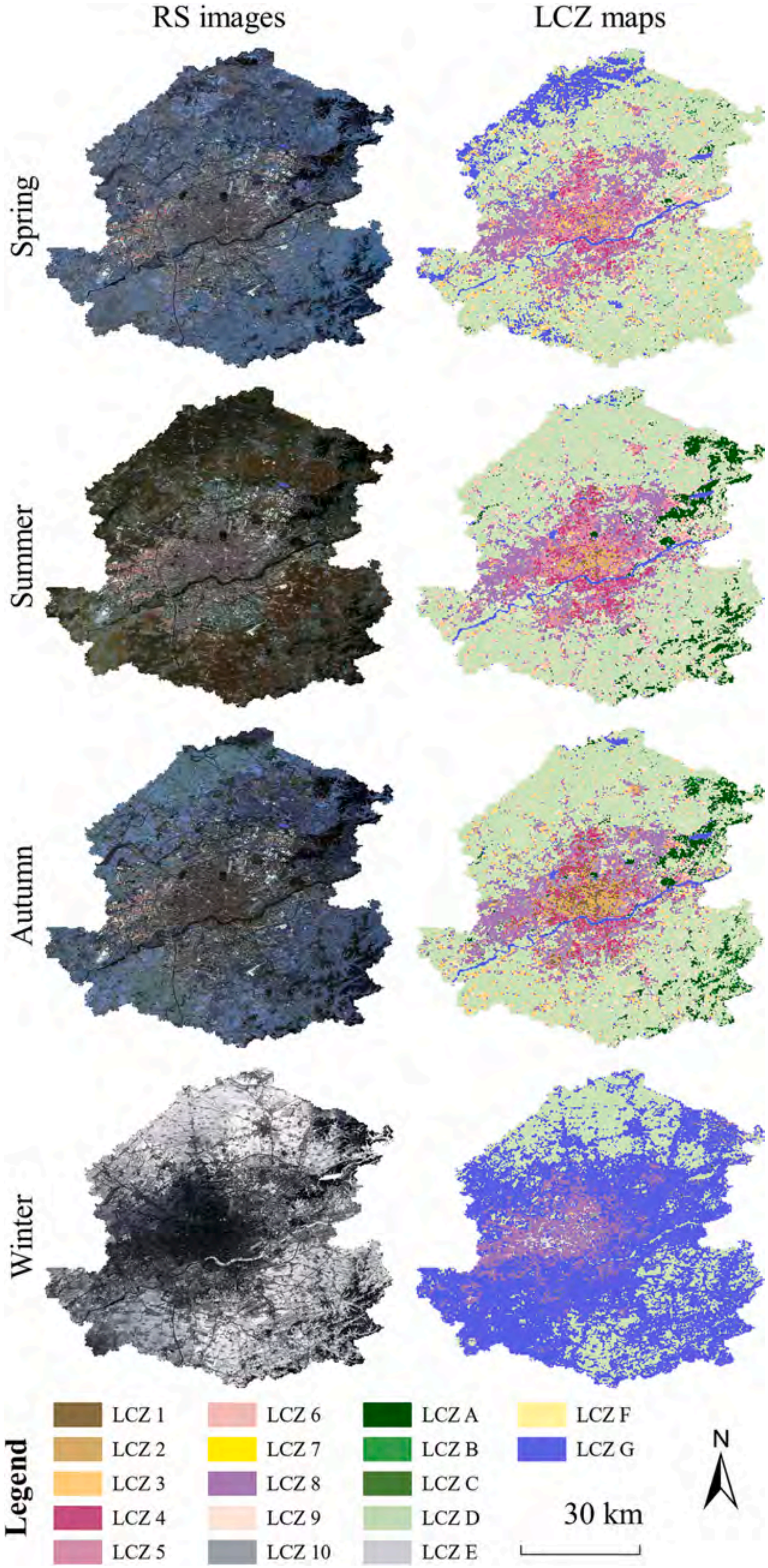

(caption on next page)

Fig. 6. RS images and prediction results for different seasons.

Table 3
Comparison of the matching degree of LCZ prediction results for different seasons.

Season	MD_{LC}	MD_{BD}	MD
Spring	0.74	0.43	0.59
Summer	0.84	0.57	0.71
Autumn	0.85	0.36	0.61
Winter	0.35	0.10	0.23

understanding of urban microclimate and will benefit future urban environment planning and climate mitigation measures (Cai et al., 2018).

At present, the 100-m-scale refined LCZ map produced by the World Urban Database and Access Portal Tools has been widely used in urban climate studies (Chen et al., 2020; Dian et al., 2020; Verdonck et al., 2017). Some researchers have also tried to achieve more refined LCZ classification by using GIS workflow (Yang et al., 2022; Xin et al., 2022; Zhang et al., 2022). Oliveira et al. (2020), Ren et al. (2022), and Yang et al. (2021a) made LCZ maps with scales ranging from 30 to 60 m and showed that different types of LCZs have different effects on the LST. The LST exhibits the strongest correlations with the floor area ratio of LCZ 2 and building height of LCZ 3. Shi et al. (2022) analyzed the effect of urban ventilation corridors on the urban heat island intensity on a 30 m LCZ map and reported that LCZ E is the largest component of ventilation corridors and the urban heat island intensity of LCZs in ventilation corridors is often

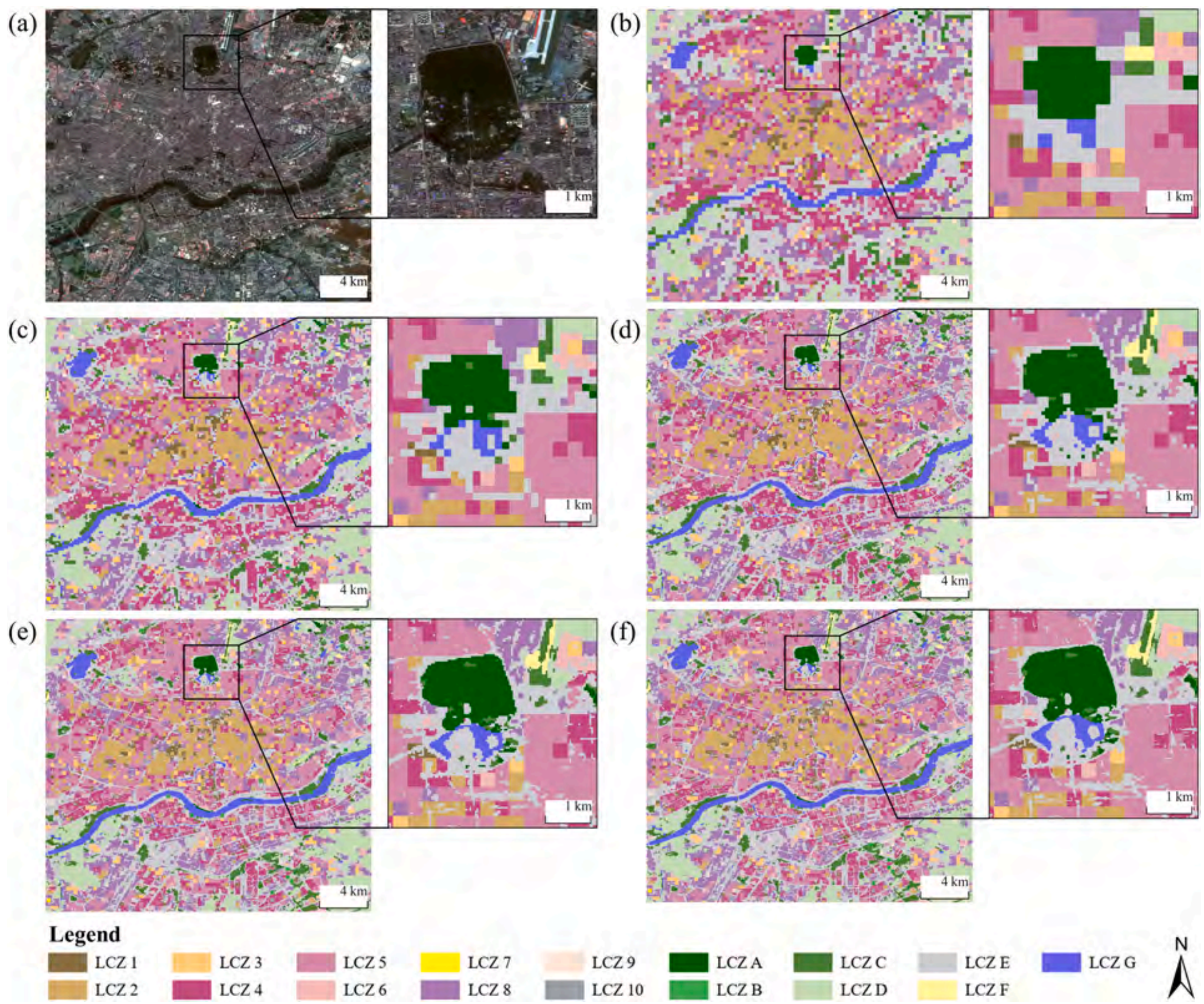

Fig. 7. Downscaling mapping results. (a) RS image; (b–f) LCZ maps with scales of 320, 160, 80, 40, and 20 m.

Table 4
Classification accuracy of LCZ maps at different scales.

Scale of LCZ Map	OA	OA_b	OA_n	OA_{type}	AA	RA	Kappa
320 m	72.22	72.41	71.86	88.33	66.22	63.87	68.26
160 m	75.56	75.67	75.36	88.89	67.65	70.15	72.16
80 m	79.44	78.90	80.28	90.00	70.89	71.89	76.58
40 m	83.33	81.65	85.92	93.33	74.55	74.70	80.99
20 m	84.44	83.49	85.92	94.44	73.75	76.37	82.29

Note: The unit of OA, OA_b, OA_n, OA_{type}, AA, AR, and Kappa is %.

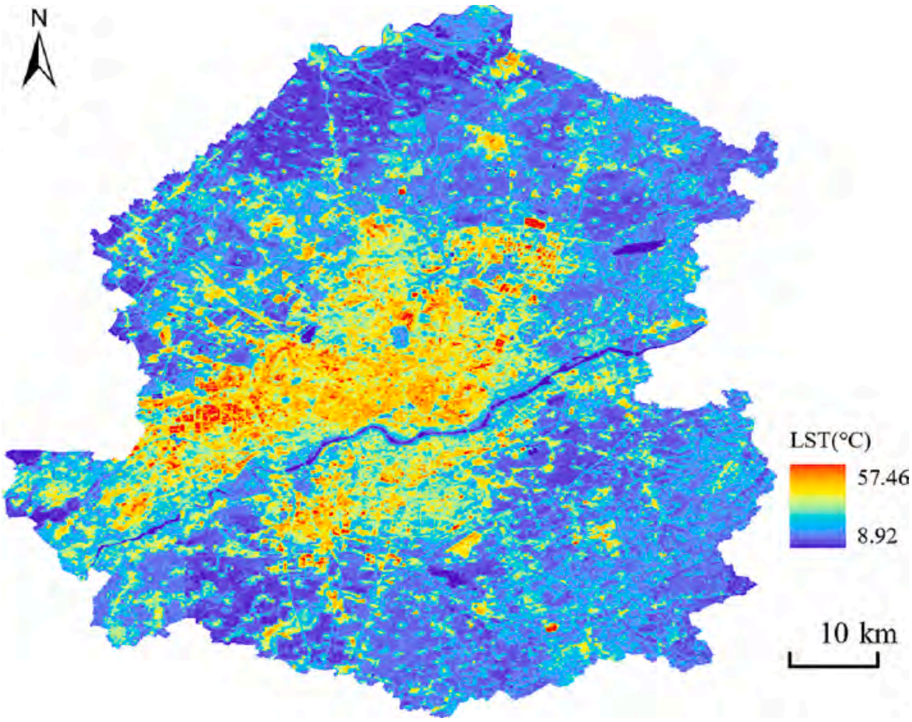

Fig. 8. Spatial distribution of the LST in the study area.

Table 5
Average LST of each LCZ at different scales.

LCZ Type	Percentage	20 m		40 m		80 m		160 m		320 m	
		Mean	std	Mean	std	Mean	std	Mean	std	Mean	std
LCZ 1	0.34-0.40	38.4	2.28	38.39	2.27	38.4	2.26	38.41	2.23	38.41	2.32
LCZ 2	1.24-1.40	41.27	2.02	41.26	2.02	41.22	2.05	41.17	2.09	40.99	2.26
LCZ 3	0.99-1.13	39.35	2.36	39.33	2.37	39.33	2.37	39.24	2.45	38.89	2.7
LCZ 4	2.23-2.65	38.04	2.23	38.02	2.23	38.00	2.23	38.01	2.23	38.03	2.28
LCZ 5	3.61-4.06	39.52	2.25	39.52	2.25	39.52	2.25	39.51	2.27	39.33	2.42
LCZ 6	4.17-4.56	36.43	2.29	36.43	2.28	36.41	2.3	36.28	2.4	35.85	2.7
LCZ 7	0.01-0.01	37.82	4.84	37.83	4.83	38.08	4.4	37.56	5.1	39.44	2.83
LCZ 8	6.24-6.63	40.63	3.65	40.64	3.64	40.65	3.63	40.58	3.66	40.3	3.8
LCZ 9	0.57-0.91	35.72	2.39	35.72	2.39	35.78	2.38	35.87	2.38	35.91	2.47
LCZ 10	0.33-0.43	39.03	2.95	39.05	2.92	39.14	2.89	39.16	2.93	39.45	3.12
LCZ A	3.83-3.86	30.59	1.03	30.59	1.04	30.6	1.07	30.63	1.13	30.67	1.23
LCZ B	0.19-0.19	33.24	2.42	33.24	2.42	33.19	2.37	33.17	2.39	33.18	2.40
LCZ C	3.93-4.40	32.59	2.75	32.59	2.75	32.59	2.78	32.58	2.8	32.64	2.98
LCZ D	51.76-53.09	31.23	2.32	31.22	2.32	31.24	2.33	31.29	2.38	31.4	2.49
LCZ E	14.96-16.93	36.07	2.96	36.04	2.94	35.95	2.93	35.82	2.98	35.69	3.13
LCZ F	0.10-0.15	38.56	4.3	38.59	4.29	38.67	4.22	38.91	4.14	38.93	4.02
LCZ G	1.97-2.44	30.6	2.44	30.58	2.42	30.57	2.44	30.54	2.51	30.51	2.51

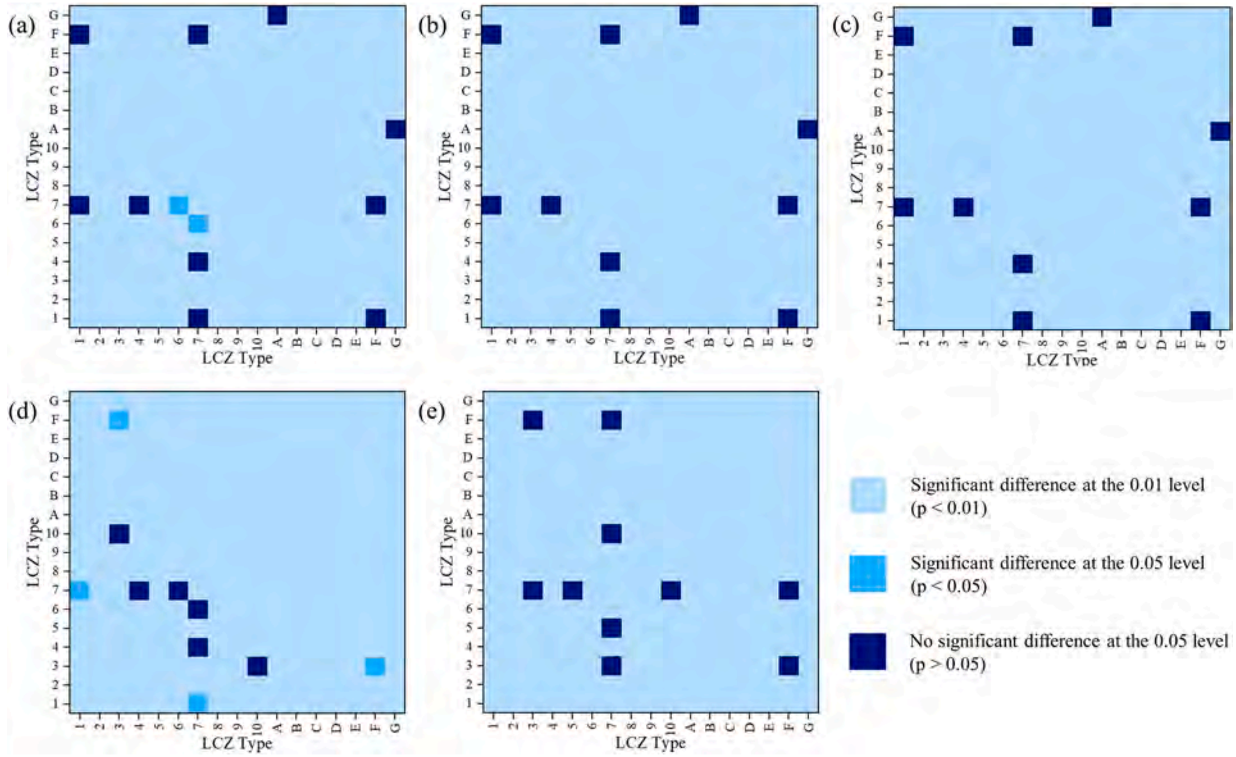

Fig. 9. Significance of the LST differences between LCZ classes under different scale grids. (a–e) Significance of differences at scales of 20, 40, 80, 160, and 320 m.

lower than that of non-corridor LCZs.

However, it is difficult to obtain high-precision refined LCZ maps using the above methods (Yoo et al., 2019; Ren et al., 2019). This is predominantly because directly creating smaller-scale grids will reduce the scene information in RS workflows and small-scale grids in GIS workflows will cause building segmentation. To achieve more precise LCZ mapping, very-high resolution (VHR) images have been applied to a refined scale in LCZ classification studies (Bartesaghi Koc et al., 2018; Zhao et al., 2019). Based on the combination with a geographic object-based image segmentation method (Chen et al., 2018), the LCZ mapping accuracy of VHR RS images reached 89%, which is substantially higher than the 69% based on Landsat 30 m resolution images (Simanjuntak et al., 2019). However, the availability of VHR images also limits the development of refined LCZ maps over a wide area.

This study has proposed a downscale process that can maintain the accuracy of LCZ classification and the ability of thermal environment feature expression, which provides a new idea for the creation of fine LCZ maps. However, the downscaling process still needs the support of building roof data. When drawing LCZ maps of long time series, it is necessary to use artificial intelligence method to recognize the building contour in the study area, which increases the complexity of the study to a certain extent.

4.2. Transferability of the downscaling process

Data used in LCZ downscaling process are mainly from deep learning LCZ basemaps, building outline vectors, and ESRI land cover data. These are all secondary products obtained by using deep learning methods for object classification and semantic segmentation of original RS images. All the data used in the downscaling process have an accuracy above 80%, providing the opportunity for global researchers to use or reproduce relevant data. Therefore, the downscaling process proposed in this study can be applied to the LCZ classification in countries or regions with different development levels and different cultures. To further improve the classification transferability of the LCZ downscaling process, global, high time resolution and high accuracy remote sensing products are still needed.

In terms of training datasets required for generating LCZ base maps, given that the metropolitan areas in the So2Sat LCZ42 label dataset are geographically separated from each other in the training set, validation set, and test set, the classification accuracy in previous studies often does not exceed 75% (Qiu et al., 2020; Wang et al., 2022; Zhou et al., 2021; Zhu et al., 2019b). In this study, the training and validation sets were remixed to improve the quality of the training samples. An overall accuracy of 83.64% was achieved and the user accuracy and producer accuracy of the built type LCZs have improved. This has shown that improving the spatial distribution of sample cities can effectively improve the classification accuracy.

The lack of complete building vector data with height information is another important factor that restricts LCZ mapping at the global scale. In previous GIS workflow LCZ mapping studies, building height information was generally provided by planning departments and often had a low temporal resolution or was incomplete. Therefore, related research also focused on urban central areas

(Geletič and Lehnert, 2016; Kotharkar and Bagade, 2018b). In the downscaling process proposed in this study, given that the height information of buildings was extracted from remote sensing images, we only needed to obtain the building density information from the building outline vectors to determine the LCZ classification of the downscale grid. Compared with detailed planning data, building outline vectors that do not provide building heights are often easier to generate automatically through deep learning methods and often have a high level of accuracy. Based on global building outline vectors such as that provided by Microsoft Bing Map (Microsoft, 2022), the downscaled LCZ mapping method proposed in this study can be applied to a wider area.

5. Conclusion

In this study, a process for downscaling the deep learning LCZ basemap based on the GIS method was proposed and the validity of the process has been verified. The results have shown that:

(1) When the width of the MSMLA model was expanded four-fold, the highest overall accuracy of 83.64% was achieved on the So2Sat LCZ42 dataset. Based on the results, that is, the highest matching degree of 0.71, summer is the most appropriate season for LCZ classification in the study area.
(2) The grids with changed LCZ types at different scales accounted for 29.34% and were predominantly distributed in the interior of the built type LCZ or at the junctions of different types of LCZs. As the downscaling multiple increased, the boundaries between different types of LCZs became smoother and more refined information about the land surface changes could be obtained.
(3) The LST levels of LCZs at each scale significantly differed ($p < 0.01$), indicating that the LCZ downscaling process has a strong ability to express the thermal characteristics of urban landscapes. At the 160 m scale, only the LSTs of 3 LCZ combinations did not significantly differ at the 0.05 level. This has shown that this scale was the most suitable for analyzing the urban thermal environment in the study area.

Given that all data used in the downscaling process are secondary products generated by artificial intelligence models, the downscaling process proposed in this study in theory has a high level of transferability. This downscaling process compensates for the inability to create fine-scale LCZ maps when ultra-high-resolution images and detailed planning data are missing and promotes a more refined analysis of urban microclimate.

CRediT authorship contribution statement

Wenbo Yu: Conceptualization, Validation, Formal analysis, Writing - review & editing. **Jun Yang:** Conceptualization, Methodology. **Feng Wu:** Funding acquisition, Resources, Software. **Huisheng Yu:** Data curation, Methodology. **Jiayi Ren:** Methodology, Writing - original draft. **Xiangming Xiao:** Supervision, Validation. **Jianhong Xia:** Supervision, Writing - review & editing.

Declaration of Competing Interest

This manuscript has not been published or presented elsewhere in part or in entirety and is not under consideration by another journal. We have read and understood your journal's policies, and we believe that neither the manuscript nor the study violates any of these. There are no conflicts of interest to declare.

Data availability

The code and tool for the downscaling process designed in this study can be downloaded from https://github.com/YuWenboNeu/LCZ_Downscaling_Mapping. The source of the data used in the downscaling process has been described in detail in the text.

Acknowladgments

This research study was supported by the National Natural Science Foundation of China (grant no's 41771178, 42030409, and 41671151), the Fundamental Research Funds for the Central Universities (grantno. N2111003), Basic Scientific Research Project (Key Project) of the Education Department of Liaoning Province (grant no. LJKZ0964), Natural Science Foundation of Guizhou Province (grant no. (2019)1150).

Appendix A. Supplementary data

Supplementary data to this article can be found online at https://doi.org/10.1016/j.uclim.2023.101500.

References

Bartesaghi Koc, C., Osmond, P., Peters, A., Irger, M., 2018. Understanding land surface temperature differences of local climate zones based on airborne remote sensing data. IEEE J. Select. Top. Appl. Earth Observ. Rem. Sens. 11, 2724–2730. https://doi.org/10.1109/JSTARS.2018.2815004.

Brousse, O., Martilli, A., Foley, M., Mills, G., Bechtel, B., 2016. WUDAPT, an efficient land use producing data tool for mesoscale models? Integration of urban LCZ in WRF over Madrid. Urban Clim. 17, 116–134. https://doi.org/10.1016/j.uclim.2016.04.001.

Cai, M., Ren, C., Xu, Y., Lau, K.K.-L., Wang, R., 2018. Investigating the relationship between local climate zone and land surface temperature using an improved WUDAPT methodology – a case study of Yangtze River Delta, China. Urban Clim. 24, 485–502. https://doi.org/10.1016/j.uclim.2017.05.010.

Chen, G., Weng, Q., Hay, G.J., He, Y., 2018. Geographic object-based image analysis (GEOBIA): emerging trends and future opportunities. GISci. Rem. Sens. 55, 159–182. https://doi.org/10.1080/15481603.2018.1426092.

Chen, X., Xu, Y., Yang, J., Wu, Z., Zhu, H., 2020. Remote sensing of urban thermal environments within local climate zones: a case study of two high-density subtropical Chinese cities. Urban Clim. 31, 100568 https://doi.org/10.1016/j.uclim.2019.100568.

Chen, G., Xie, J., Li, W., Li, X., Hay Chung, L.C., Ren, C., Liu, X., 2021. Future "local climate zone" spatial change simulation in Greater Bay Area under the shared socioeconomic pathways and ecological control line. Build. Environ. 203, 108077 https://doi.org/10.1016/j.buildenv.2021.108077.

Chen, Y., Yang, J., Yu, W., Ren, J., Xiao, X., Xia, J.C., 2023. Relationship between urban spatial form and seasonal land surface temperature under different grid scales. Sustainable Cities and Society 89, 104374. https://doi.org/10.1016/j.scs.2022.104374.

Ching, J., Aliaga, D., Mills, G., Masson, V., See, L., Neophytou, M., Middel, A., Baklanov, A., Ren, C., Ng, E., Fung, J., Wong, M., Huang, Y., Martilli, A., Brousse, O., Stewart, I., Zhang, X., Shehata, A., Miao, S., Wang, X., Wang, W., Yamagata, Y., Duarte, D., Li, Y., Feddema, J., Bechtel, B., Hidalgo, J., Roustan, Y., Kim, Y., Simon, H., Kropp, T., Bruse, M., Lindberg, F., Grimmond, S., Demuzure, M., Chen, F., Li, C., Gonzales-Cruz, J., Bornstein, B., He, Q., Tzu-Ping, Hanna A., Erell, E., Tapper, N., Mall, R.K., Niyogi, D., 2019. Pathway using WUDAPT's digital Synthetic City tool towards generating urban canopy parameters for multi-scale urban atmospheric modeling. Urban Clim. 28, 100459 https://doi.org/10.1016/j.uclim.2019.100459.

Demuzere, M., Bechtel, B., Middel, A., Mills, G., 2019. Mapping Europe into local climate zones. PLoS One 14, e0214474. https://doi.org/10.1371/journal.pone.0214474.

Demuzere, M., Hankey, S., Mills, G., Zhang, W., Lu, T., Bechtel, B., 2020. Combining expert and crowd-sourced training data to map urban form and functions for the continental US. Sci. Data 7, 1–13. https://doi.org/10.1038/s41597-020-00605-z.

Dian, C., Pongrácz, R., Dezső, Z., Bartholy, J., 2020. Annual and monthly analysis of surface urban heat island intensity with respect to the local climate zones in Budapest. Urban Clim. 31, 100573 https://doi.org/10.1016/j.uclim.2019.100573.

Ellefsen, R., 1991. Mapping and measuring buildings in the canopy boundary layer in ten U.S. cities. Energy Build. 16, 1025–1049. https://doi.org/10.1016/0378-7788(91)90097-M.

Esch, T., Marconcini, M., Felbier, A., Roth, A., Heldens, W., Huber, M., Schwinger, M., Taubenboeck, H., Mueller, A., Dech, S., 2013. Urban footprint processor-fully automated processing chain generating settlement masks from global data of the TanDEM-X mission. IEEE Geosci. Remote Sens. Lett. 10, 1617–1621. https://doi.org/10.1109/LGRS.2013.2272953.

Estacio, I., Babaan, J., Pecson, N.J., Blanco, A.C., Escoto, J.E., Alcantara, C.K., 2019. GIS-based mapping of local climate zones using fuzzy logic and cellular automata. Int. Arch. Photogramm. Remote. Sens. Spat. Inf. Sci. XLII-4/W19, 199–206. https://doi.org/10.5194/isprs-archives-XLII-4-W19-199-2019.

Gal, T., Unger, J., 2009. Detection of ventilation paths using high-resolution roughness parameter mapping in a large urban area. Build. Environ. 44, 198–206. https://doi.org/10.1016/j.buildenv.2008.02.008.

Geletič, J., Lehnert, M., 2016. GIS-based delineation of local climate zones: the case of medium-sized central European cities. Moravian Geogr. Rep. 24, 2–12. https://doi.org/10.1515/mgr-2016-0012.

He, B.-J., Zhao, Z.-Q., Shen, L.-D., Wang, H.-B., Li, L.-G., 2019. An approach to examining performances of cool/hot sources in mitigating/enhancing land surface temperature under different temperature backgrounds based on landsat 8 image. Sustain. Cities Soc. 44, 416–427. https://doi.org/10.1016/j.scs.2018.10.049.

Jarvi, L., Havu, M., Ward, H.C., Bellucco, V., McFadden, J.P., Toivonen, T., Heikinheimo, V., Kolari, P., Riikonen, A., Grimmond, C.S.B., 2019. Spatial modeling of local-scale biogenic and anthropogenic carbon dioxide emissions in Helsinki. J. Geophys. Res.-Atmos. 124, 8363–8384. https://doi.org/10.1029/2018JD029576.

Karra, K., Kontgis, C., Statman-Weil, Z., Mazzariello, J.C., Mathis, M., Brumby, S.P., 2021. Global land use / land cover with Sentinel 2 and deep learning. In: 2021 IEEE International Geoscience and Remote Sensing Symposium IGARSS. Presented at the 2021 IEEE International Geoscience and Remote Sensing Symposium IGARSS, pp. 4704–4707. https://doi.org/10.1109/IGARSS47720.2021.9553499.

Kim, M., Jeong, D., Kim, Y., 2021. Local climate zone classification using a multi-scale, multi-level attention network. ISPRS J. Photogramm. Remote Sens. 181, 345–366. https://doi.org/10.1016/j.isprsjprs.2021.09.015.

Kotharkar, R., Bagade, A., 2018a. Evaluating urban heat island in the critical local climate zones of an Indian city. Landsc. Urban Plan. 169, 92–104. https://doi.org/10.1016/j.landurbplan.2017.08.009.

Kotharkar, R., Bagade, A., 2018b. Local climate zone classification for Indian cities: a case study of Nagpur. Urban Clim. 24, 369–392. https://doi.org/10.1016/j.uclim.2017.03.003.

Lau, K., Chao, R., Yuan, S., Zheng, V., Lai, D., 2015. Determining the optimal size of local climate zones for spatial mapping in high-density cities. In: The 9th International Conference on Urban Climate (ICUC9).

Leconte, F., Bouyer, J., Claverie, R., Pétrissans, M., 2015. Using local climate zone scheme for UHI assessment: evaluation of the method using mobile measurements. Build. Environ. Spec. Issue: Clim. Adapt. Cities 83, 39–49. https://doi.org/10.1016/j.buildenv.2014.05.005.

Lelovics, E., Unger, J., Gal, T., Gal, C.V., 2014. Design of an urban monitoring network based on local climate zone mapping and temperature pattern modelling. Clim. Res. 60, 51–62. https://doi.org/10.3354/cr01220.

Li, H., Zhou, Y., Li, X., Meng, L., Wang, X., Wu, S., Sodoudi, S., 2018. A new method to quantify surface urban heat island intensity. Sci. Total Environ. 624, 262–272. https://doi.org/10.1016/j.scitotenv.2017.11.360.

Li, X., Zhou, Y., Yu, S., Jia, G., Li, H., Li, W., 2019. Urban heat island impacts on building energy consumption: a review of approaches and findings. Energy 174, 407–419. https://doi.org/10.1016/j.energy.2019.02.183.

Li, N., Yang, J., Qiao, Z., Wang, Y., Miao, S., 2021. Urban thermal characteristics of local climate zones and their mitigation measures across cities in different climate zones of China. Remote Sens. 13, 1468. https://doi.org/10.3390/rs13081468.

Liang, Z., Huang, J., Wang, Y., Wei, F., Wu, S., Jiang, H., Zhang, X., Li, S., 2021. The mediating effect of air pollution in the impacts of urban form on nighttime urban heat island intensity. Sustain. Cities Soc. 74, 102985 https://doi.org/10.1016/j.scs.2021.102985.

Liu, S., Shi, Q., 2020. Local climate zone mapping as remote sensing scene classification using deep learning: a case study of metropolitan China. ISPRS J. Photogramm. Remote Sens. 164, 229–242. https://doi.org/10.1016/j.isprsjprs.2020.04.008.

Ma, L., Zhu, X., Qiu, C., Blaschke, T., Li, M., 2021. Advances of local climate zone mapping and its practice using object-based image analysis. Atmosphere 12, 1146. https://doi.org/10.3390/atmos12091146.

Masó, J., Serral, I., Domingo-Marimon, C., Zabala, A., 2019. Earth observations for sustainable development goals monitoring based on essential variables and driver-pressure-state-impact-response indicators. Int. J. Digit. Earth 1–19.

Microsoft, 2022. microsoft/GlobalMLBuildingFootprints.

Oliveira, A., Lopes, A., Niza, S., 2020. Local climate zones in five southern European cities: an improved GIS-based classification method based on Copernicus data. Urban Clim. 33, 100631 https://doi.org/10.1016/j.uclim.2020.100631.

Qiu, C., Tong, X., Schmitt, M., Bechtel, B., Zhu, X.X., 2020. Multilevel feature fusion-based CNN for local climate zone classification from Sentinel-2 images: benchmark results on the So2Sat LCZ42 dataset. IEEE J. Sel. Top. Appl. Earth Observ. Rem. Sens. 13, 2793–2806. https://doi.org/10.1109/JSTARS.2020.2995711.

Qiu, C., Liebel, L., Hughes, L.H., Schmitt, M., Körner, M., Zhu, X.X., 2022. Multitask learning for human settlement extent regression and local climate zone classification. IEEE Geosci. Remote Sens. Lett. 19, 1–5. https://doi.org/10.1109/LGRS.2020.3037246.

Quan, J., 2019. Enhanced geographic information system-based mapping of local climate zones in Beijing, China. Sci. China Technol. Sci. 62, 2243–2260. https://doi.org/10.1007/s11431-018-9417-6.
Quan, S.J., Bansal, P., 2021. A systematic review of GIS-based local climate zone mapping studies. Build. Environ. 196, 107791 https://doi.org/10.1016/j.buildenv.2021.107791.
Ren, C., Cai, M., Li, X., Zhang, L., Wang, R., Xu, Y., Ng, E., 2019. Assessment of local climate zone classification maps of cities in China and feasible refinements. Sci. Rep. 9, 18848. https://doi.org/10.1038/s41598-019-55444-9.
Ren, J., Yang, J., Zhang, Y., Xiao, X., Xia, J.C., Li, X., Wang, S., 2022. Exploring thermal comfort of urban buildings based on local climate zones. J. Clean. Prod. 340, 130744 https://doi.org/10.1016/j.jclepro.2022.130744.
Rosentreter, J., Hagensieker, R., Waske, B., 2020. Towards large-scale mapping of local climate zones using multitemporal sentinel 2 data and convolutional neural networks. Remote Sens. Environ. 237, 111472 https://doi.org/10.1016/j.rse.2019.111472.
Shi, Z., Yang, J., Zhang, Y., Xiao, X., Xia, J.C., 2022. Urban ventilation corridors and spatiotemporal divergence patterns of urban heat island intensity: a local climate zone perspective. Environ. Sci. Pollut. Res. https://doi.org/10.1007/s11356-022-21037-9.
Simanjuntak, R.M., Kuffer, M., Reckien, D., 2019. Object-based image analysis to map local climate zones: the case of Bandung, Indonesia. Appl. Geogr. 106, 108–121. https://doi.org/10.1016/j.apgeog.2019.04.001.
Skarbit, N., Stewart, I.D., Unger, J., Gál, T., 2017. Employing an urban meteorological network to monitor air temperature conditions in the 'local climate zones' of Szeged, Hungary. Int. J. Climatol. 37, 582–596. https://doi.org/10.1002/joc.5023.
Stepani, H.M.N., Emmanuel, R., 2022. How much green is really "cool"? Target setting for thermal comfort enhancement in a warm, Humid City (Jakarta, Indonesia). Atmosphere 13, 184. https://doi.org/10.3390/atmos13020184.
Stewart, I.D., Oke, T.R., 2012. Local climate zones for Urban temperature studies. Bull. Am. Meteorol. Soc. 93, 1879–1900. https://doi.org/10.1175/BAMS-D-11-00019.1.
Stewart, I.D., Oke, T.R., Krayenhoff, E.S., 2014. Evaluation of the "local climate zone" scheme using temperature observations and model simulations. Int. J. Climatol. 34, 1062–1080. https://doi.org/10.1002/joc.3746.
Stokes, E.C., Seto, K.C., 2019. Characterizing urban infrastructural transitions for the sustainable development goals using multi-temporal land, population, and nighttime light data. Remote Sens. Environ. 234, 111430 https://doi.org/10.1016/j.rse.2019.111430.
Unger, J., Lelovics, E., Gál, T., 2014. Local climate zone mapping using GIS methods in Szeged. Hungar. Geograph. Bull. 63, 29–41. https://doi.org/10.15201/hungeobull.63.1.3.
United Nations, 2015. THE 17 GOALS | Sustainable Development [WWW Document]. URL. https://sdgs.un.org/goals (accessed 10.13.22).
Vanos, J.K., Kalkstein, L.S., Sanford, T.J., 2015. Detecting synoptic warming trends across the US Midwest and implications to human health and heat-related mortality. Int. J. Climatol. 35, 85–96. https://doi.org/10.1002/joc.3964.
Verdonck, M.-L., Okujeni, A., van der Linden, S., Demuzere, M., De Wulf, R., Van Coillie, F., 2017. Influence of neighbourhood information on 'local climate zone' mapping in heterogeneous cities. Int. J. Appl. Earth Obs. Geoinf. 62, 102–113. https://doi.org/10.1016/j.jag.2017.05.017.
Voogt, J., 2021. Urban heatwaves and thermal remote sensing. In: 2021 IEEE International Geoscience and Remote Sensing Symposium IGARSS. Presented at the 2021 IEEE International Geoscience and Remote Sensing Symposium IGARSS, pp. 938–941. https://doi.org/10.1109/IGARSS47720.2021.9554528.
Wang, R., Wang, M., Zhang, Z., Xing, J., Liu, X., 2022. LLNet: lightweight network with a channel and spatial attention mechanism for local climate zone classification from Sentinel-2 image. Int. J. Climatol. https://doi.org/10.1002/joc.7932.
Woodruff, S.C., Meerow, S., Stults, M., Wilkins, C., 2022. Adaptation to resilience planning: alternative pathways to prepare for climate change. J. Plan. Educ. Res. 42, 64–75. https://doi.org/10.1177/0739456X18801057.
Yang, X., Peng, L.L.H., Jiang, Z., Chen, Y., Yao, L., He, Y., Xu, T., 2020a. Impact of urban heat island on energy demand in buildings: local climate zones in Nanjing. Appl. Energy 260, 114279. https://doi.org/10.1016/j.apenergy.2019.114279.
Yang, J., Wang, Y., Xiu, C., Xiao, X., Xia, J., Jin, C., 2020b. Optimizing local climate zones to mitigate urban heat island effect in human settlements. J. Clean. Prod. 275, 123767 https://doi.org/10.1016/j.jclepro.2020.123767.
Yang, J., Ren, J., Sun, D., Xiao, X., Xia, J., Jin, C., Li, X., 2021a. Understanding land surface temperature impact factors based on local climate zones. Sustain. Cities Soc. 69, 102818 https://doi.org/10.1016/j.scs.2021.102818.
Yang, J., Yang, Y., Sun, D., Jin, C., Xiao, X., 2021b. Influence of urban morphological characteristics on thermal environment. Sustain. Cities Soc. 72, 103045 https://doi.org/10.1016/j.scs.2021.103045.
Yang, J., Xin, J., Zhang, Y., Xiao, X., Xia, J.C., 2022. Contributions of sea–land breeze and local climate zones to daytime and nighttime heat island intensity. NPJ Urban Sustain. 2, 1–11. https://doi.org/10.1038/s42949-022-00055-z.
Yoo, C., Han, D., Im, J., Bechtel, B., 2019. Comparison between convolutional neural networks and random forest for local climate zone classification in mega urban areas using Landsat images. ISPRS J. Photogramm. Remote Sens. 157, 155–170. https://doi.org/10.1016/j.isprsjprs.2019.09.009.
Yoo, C., Lee, Y., Cho, D., Im, J., Han, D., 2020. Improving local climate zone classification using incomplete building data and sentinel 2 images based on convolutional neural networks. Remote Sens. 12, 3552. https://doi.org/10.3390/rs12213552.
Yu, W., Yang, J., Wu, F., He, B., Xue, B., Wang, S., Yu, H., Xiao, X., Xia, J. (Cecilia), 2023. Realistic characteristics and driving mechanisms of pseudo-human settlements in Chinese cities. Humanit Soc. Sci. Commun. 10, 1–13. https://doi.org/10.1057/s41599-023-01551-y.
Zhang, Y., 2020. The map is not the territory: coevolution of technology and institution for a sustainable future. In: Current Opinion in Environmental Sustainability, Open Issue 2020 Part A: Technology Innovations and Environmental Sustainability in the Anthropocene, 45, pp. 56–68. https://doi.org/10.1016/j.cosust.2020.08.017.
Zhang, Z., Qian, Z., Zhong, T., Chen, M., Zhang, K., Yang, Y., Zhu, R., Zhang, F., Zhang, H., Zhou, F., Yu, J., Zhang, B., Lü, G., Yan, J., 2022. Vectorized rooftop area data for 90 cities in China. Sci. Data 9, 1–12. https://doi.org/10.1038/s41597-022-01168-x.
Zhao, Z.-Q., He, B.-J., Li, L.-G., Wang, H.-B., Darko, A., 2017. Profile and concentric zonal analysis of relationships between land use/land cover and land surface temperature: case study of Shenyang, China. Energy Build. 155, 282–295. https://doi.org/10.1016/j.enbuild.2017.09.046.
Zhao, C., Jensen, J., Weng, Q., Currit, N., Weaver, R., 2019. Application of airborne remote sensing data on mapping local climate zones: cases of three metropolitan areas of Texas, U.S. Comput. Environ. Urban. Syst. 74, 175–193. https://doi.org/10.1016/j.compenvurbsys.2018.11.002.
Zhao, Z., Sharifi, A., Dong, X., Shen, L., He, B.-J., 2021. Spatial variability and temporal heterogeneity of surface urban Heat Island patterns and the suitability of local climate zones for land surface temperature characterization. Remote Sens. 13, 4338. https://doi.org/10.3390/rs13214338.
Zheng, Y., Ren, C., Xu, Y., Wang, R., Ho, J., Lau, K., Ng, E., 2018. GIS-based mapping of local climate zone in the high-density city of Hong Kong. Urban Clim. 24, 419–448. https://doi.org/10.1016/j.uclim.2017.05.008.
Zhou, Y., Li, X., Asrar, G.R., Smith, S.J., Imhoff, M., 2018. A global record of annual urban dynamics (1992–2013) from nighttime lights. Remote Sens. Environ. 219, 206–220. https://doi.org/10.1016/j.rse.2018.10.015.
Zhou, Y., Wei, T., Zhu, X., Collin, M., 2021. A parcel-based deep-learning classification to map local climate zones from Sentinel-2 images. IEEE J. Select. Top. Appl. Earth Observ. Rem. Sens. 14, 4194–4204. https://doi.org/10.1109/JSTARS.2021.3071577.
Zhu, X.X., Hu, J., Qiu, C., Shi, Y., Kang, J., Mou, L., Bagheri, H., Häberle, M., Hua, Y., Huang, R., Hughes, L., Li, H., Sun, Y., Zhang, G., Han, S., Schmitt, M., Wang, Y., 2019a. So2Sat LCZ42: A Benchmark Dataset for Global Local Climate Zones Classification arXiv:1912.12171 [cs, eess].
Zhu, Z., Zhou, Y., Seto, K.C., Stokes, E.C., Deng, C., Pickett, S.T.A., Taubenböck, H., 2019b. Understanding an urbanizing planet: strategic directions for remote sensing. Remote Sens. Environ. 228, 164–182. https://doi.org/10.1016/j.rse.2019.04.020.
Ren, J., Yang, J., Wu, F., Sun, W., Xiao, X., Xia, J. (Cecilia), 2023. Regional thermal environment changes: Integration of satellite data and land use/land cover. iScience 26, 105820. https://doi.org/10.1016/j.isci.2022.105820.

Xin, J., Yang, J., Jiang, Y., Shi, Z., Jin, C., Xiao, X., Xia, J. (Cecilia), Yang, R., 2023. Variations of Urban Thermal Risk with Local Climate Zones. Int. J. Environ. Res. Public Health 20, 3283. https://doi.org/10.3390/ijerph20043283.

Xin, J., Yang, J., Wang, L., Jin, C., Xiao, X., Xia, J. (Cecilia), 2022. Seasonal differences in the dominant factors of surface urban heat islands along the urban-rural gradient. Front. Environ. Sci 10. https://doi.org/10.3389/fenvs.2022.974811.

Zhang, R., Yang, J., Sun, D., Ma, X., Yu, W., Xiao, X., Xia, J. (Cecilia), 2022. Warming and cooling effects of local climate zones on urban thermal environment. Front. Public Health 10.